Volume 196, issues 13–16, Published 1 March 2007 ISSN 0045-7825

Computer methods in applied mechanics and engineering

Available online at
ScienceDirect
www.sciencedirect.com

http://www.elsevier.com/locate/cma

Available online at www.sciencedirect.com
ScienceDirect
Comput. Methods Appl. Mech. Engrg. 196 (2007) 1958–1967
Computer methods in applied mechanics and engineering
www.elsevier.com/locate/cma

A subdomain collocation method based on Voronoi domain partition and reproducing kernel approximation

J.X. Zhou [a,*], M.E. Li [b], Z.Q. Zhang [a], W. Zou [a], L. Zhang [a]

[a] Department of Aerospace Engineering, School of Aerospace, Xi'an Jiaotong University, Xi'an 710049, PR China
[b] School of Material Science and Engineering, Xi'an Jiaotong University, Xi'an 710049, PR China

Received 29 July 2005; received in revised form 20 March 2006; accepted 21 October 2006

Abstract

A subdomain collocation reproducing kernel approximation method is proposed. Subdomains are constructed by nonoverlapping Voronoi cells and a local weak form is defined over these subdomains. The standard RKPM shape functions are used directly for approximation, while weighting functions of the subdomain collocation method hold a constant value of unit only over a specific Voronoi cell. The body integration of the local weak form is now converted into much cheaper and efficient contour integration along the boundaries of Voronoi cells. It does not need to impose traction free boundary conditions explicitly in contrast to point collocation method. Furthermore, the method provides a natural background structure for performing h-adaptivity analysis straightforwardly. All these features constitute the subdomain collocation method a promising alternative to standard Galerkin method and point collocation method. Some elastostatics examples are presented to demonstrate the effectiveness, the convergence property, and the adaptivity performance of present method.

Keywords: Meshless method; Subdomain collocation; Reproducing kernel approximation; Voronoi diagram

1. Introduction

Meshless methods can be classified collectively as Galerkin meshless method, Petrov–Galerkin meshless method and collocation meshless method. Most of meshless methods like EFG [1], RKPM [2], PU [3] and so on fall into the first group and these Galerkin meshless methods are dominant in published literature. The MLPG [4] can be divided into the second group. Besides these two groups of meshless methods, SPH [5], HP-cloud [6], the point collocation RKPM [7] and the collocation meshless method with radial basis functions [8] are considered as the third group of meshless method, the collocation meshless method. More specifically, the above-mentioned collocation meshless methods are point collocation methods. The MLPG starts from a local weak form over a set of overlapping subdomains rather than from a global weak form which is the starting point of most of conventional Galerkin meshless method or finite element method. In the sense of satisfying governing equations in a locally way of making weighted residual zero over a subdomain, MLPG can be viewed as a subdomain collocation method. But the weighting functions used in MLPG are some kind of partition of unity interpolation functions such as MLS, Shepard and PU functions, and these functions do not hold constant over each subdomain and the method, therefore, is not the standard subdomain collocation method defined in [9]. The most prominent feature of MLPG is that it is a truly meshless method, but there are some difficulties in the numerical integration of weak form in MLPG especially when the integration region intersecting with the global boundaries [4]. A mapping is needed to transfer irregularly shaped subdomain into regularly shaped subdomain. This adds the cost of numerical integration and the difficulty of implementation of MLPG. For the situations with local concave boundaries, the mapping or the transformation would be very difficult.

* Corresponding author. Tel.: +86 29 82663929; fax: +86 29 82669044.
E-mail address: jxzhouxx@mail.xjtu.edu.cn (J.X. Zhou).

0045-7825/$ - see front matter © 2006 Elsevier B.V. All rights reserved.
doi:10.1016/j.cma.2006.10.011

Point collocation methods are the simplest meshless methods featuring straightforward implementation, direct and straightforward imposition of boundary conditions and particularly truly meshless. The point collocation methods, however, require the calculation of higher-order derivatives that would be a burden and typically not be required in a Galerkin method. In addition, in collocation methods, even the zero prescribed traction conditions need to be explicitly enforced, which constitutes a big contrast to standard Galerkin methods. From the available point collocation literature, it is noted that the accuracy of the collocation method is less than that of the Galerkin method [7,8].

In this paper, a subdomain collocation method using reproducing kernel approximation and a domain partition technique based on Voronoi diagram is presented. The method lays its basis on the reliable and high quality construction of a Voronoi diagram for even a multiply connected domain with complicated boundaries. We use a divide-and-conquer and incremental Delaunay algorithm to construct a Voronoi diagram [10,11]. Actually, there are some other researchers who use Voronoi diagrams in meshless methods for various purposes. Dolbow and Belytschko [12] used Voronoi cells to integrate the dilatational part of the weak form by a nodal quadrature technique when a mixed variational principle and a selective reduced integration were used to eliminate the volumetric locking of EFG. The nodal quadrature weights are determined from the corresponding Voronoi cell Volumes. The hydrostatic pressure variable is approximated via another set of shape functions constructed purposely to represent a constant field over each Voronoi cell. This additional set of shape functions are the same as the weighting functions used in this paper. Chen et al. [13] introduced Voronoi diagram into Galerkin meshless method and proposed a Stabilized Conforming Nodal Integration (SCNI) method and later developed it into a nonlinear version [14]. The meshless method using SCNI can stabilize spurious modes arising from nodal integration and can enhance the numerical performance of the direct nodal integration. Numerical results show that SCNI is rather efficient and more accurate than Gaussian integration. Zhou et al. [15] also used Voronoi diagrams to compute nodal volumes accurately for nodal integration of Galerkin meshless method and ultimately to improve the accuracy of nodal integration.

In present method, the trial function is approximated via standard RKPM shape functions, while the test function is evaluated by a set of constant valued weighting functions defined over a specific Voronoi cell. Therefore, the proposed method maintains the property of standard subdomain collocation. By employing the divergence theorem, the body integration which is a key issue in Galerkin meshless method is converted into a boundary integration, which is much cheaper and more computationally efficient. Meanwhile, the proposed method offers the following two features as compared with point collocation method: it is not required to calculate higher-order derivatives of shape functions; free boundaries are not necessitated to be treated explicitly as in a point collocation method.

The outline of the paper is as follows. The reproducing kernel approximation is briefly reviewed in Section 2. The formulations of subdomain collocation method for the Laplace equation and the linear elasticity problem are derived in Section 3. A detailed numerical investigation is performed and the results are presented in Section 4. Conclusions and future work are discussed in Section 5.

2. Reproducing kernel approximation

The reproducing kernel approximation starts from the corrected kernel approximation and can be written as

$$u^a(x,y) = \int_\Omega \varpi_d(x-s,y-t)u(s,t)\,\mathrm{d}s\,\mathrm{d}t. \tag{1}$$

In above and what follows, we use only two-dimensional expressions but this does not imply a loss of generality. $\varpi_d(x-s,y-t)$ is the corrected kernel function which can be expressed as

$$\varpi_d(x-s,y-t) = C(x,y,s,t)\omega_d(x-s,y-t), \tag{2}$$

where $\omega_d(x-s,y-t)$ is the conventional kernel function. The correction function $C(x,y,s,t)$ can be expressed as a linear polynomial function and the coefficients and their derivatives of basis function can be obtained analytically in terms of kernel function moments [16,17]. For the C^0 problems in which only a linear consistency requirement is needed, the correction function has the following form:

$$C(x,y,s,t) = c_0(x,y) + c_1(x,y)(x-s) + c_2(x,y)(y-t), \tag{3}$$

and the explicit expressions of correction coefficients are as follows [16]:

$$c_0 = (m_{02}m_{20} - m_{11}^2)/\Delta, \tag{4}$$

$$c_1 = (m_{01}m_{11} - m_{02}m_{10})/\Delta, \tag{5}$$

$$c_2 = (m_{10}m_{11} - m_{01}m_{20})/\Delta, \tag{6}$$

where

$$m_{ij}(x,y) = \int_\Omega (x-s)^i(y-t)^j w_d(x-s,y-t)\,\mathrm{d}s\,\mathrm{d}t \tag{7}$$

are kernel function moments, Δ is the determinant of a 3×3 moment matrix $\mathbf{M}$ and is given as

$$\Delta = m_{00}m_{20}m_{02} + m_{10}m_{11}m_{01} + m_{01}m_{10}m_{11} - m_{01}^2m_{20} - m_{10}^2m_{02} - m_{11}^2m_{00}. \tag{8}$$

The derivatives of correction coefficients can also be expressed analytically and details can be found in [16] for two-dimensional and [17] for three-dimensional problems. The goal of these explicit manipulations of reproducing kernel approximation is to speed up the evaluation of RKPM shape functions.

If a trapezoidal ruler is applied to Eq. (1), one yields the discretized form of Eq. (1) which is referred to as the

Reproducing Kernel Particle Method (RKPM) in the following form:

$$u^a(x,y) = \sum_{I=1}^{\mathrm{NP}} N_I(x,y)u_I, \tag{9}$$

where $N_I(x,y) = C(x-x_I, y-y_I)w_d(x-x_I, y-y_I)\Delta V_I$ is defined as the RKPM shape function for node I, u_I is the nodal parameter associated with node I, ΔV_I is the nodal volume (area for two dimensions) of node I, and NP is the total node number to discretize the problem domain.

3. Subdomain collocation method

In order to illustrate the main idea of the present method, we start with derivation of subdomain method for the Laplace equation and then develop the formulations into linear elasticity problems.

3.1. Subdomain collocation method for Laplace equation with Dirichlet and Neumann boundary conditions

For the Laplace equation with Dirichlet and Neumann boundary conditions, the governing equation is

$$\frac{\partial^2 u}{\partial x^2} + \frac{\partial^2 u}{\partial y^2} = 0, \quad 0 < x < 1, \ 0 < y < 1. \tag{10}$$

The cubic exact solution is given by

$$u(x,y) = -x^3 - y^3 + 3xy^2 + 3x^2y. \tag{11}$$

The Dirichlet and Neumann boundary conditions are summarized as

$$\bar{u}(x=0) = -y^3, \tag{12}$$

$$\bar{u}(x=1) = -1 - y^3 + 3y^2 + 3y, \tag{13}$$

$$\frac{\partial \bar{u}}{\partial y}(y=0) = 3x^2, \tag{14}$$

$$\frac{\partial \bar{u}}{\partial y}(y=1) = -3 + 6x + 3x^2. \tag{15}$$

Applying weighted residual approach for the Ith subdomain Ω_s^I and using penalty method to impose Dirichlet boundaries on Γ_{su}^I gives the following augmented local weak form:

$$\int_{\Omega_s^I} \left(\frac{\partial^2 u}{\partial x^2} + \frac{\partial^2 u}{\partial y^2}\right)\delta u \,\mathrm{d}\Omega + \alpha \int_{\Gamma_{su}^I} (u-\bar{u})\delta u \,\mathrm{d}\Gamma = 0, \tag{16}$$

where α is the penalty parameter, δu is a variation and $\bar{u}$ is the prescribed value on Γ_{su}^I, the intersection of the local boundary and the global Dirichlet boundary. Employing divergence theorem to the first part of the integration in Eq. (16), one obtains

$$\int_{\Gamma_s^I} \left(\frac{\partial u}{\partial x}n_x + \frac{\partial u}{\partial y}n_y\right)\delta u \,\mathrm{d}\Gamma - \int_{\Omega_s^I} \left(\frac{\partial u}{\partial x}\frac{\partial \delta u}{\partial x} + \frac{\partial u}{\partial y}\frac{\partial \delta u}{\partial y}\right)\mathrm{d}\Omega + \alpha \int_{\Gamma_{su}^I} (u-\bar{u})\delta u \,\mathrm{d}\Gamma = 0 \tag{17}$$

in which n_x and n_y are the outward unit normal to the local boundary Γ_s^I which is subordinate to subdomain Ω_s^I and $\Gamma_s^I = \Gamma_{si}^I \cup \Gamma_{su}^I \cup \Gamma_{st}^I$. Here Γ_{st}^I denotes the intersection of local boundary and the global Neumann boundary and Γ_{si}^I is the remaining local boundary of Γ_s^I except Γ_{su}^I and Γ_{st}^I. Dividing the first integral of Eq. (17) into several parts according to different boundary conditions produces

$$\int_{\Gamma_{si}^I + \Gamma_{su}^I} \left(\frac{\partial u}{\partial x}n_x + \frac{\partial u}{\partial y}n_y\right)\delta u \,\mathrm{d}\Gamma + \int_{\Gamma_{st}^I} \left(\frac{\partial \bar{u}}{\partial x}n_x + \frac{\partial \bar{u}}{\partial y}n_y\right)\delta u \,\mathrm{d}\Gamma - \int_{\Omega_s^I} \left(\frac{\partial u}{\partial x}\frac{\partial \delta u}{\partial x} + \frac{\partial u}{\partial y}\frac{\partial \delta u}{\partial y}\right)\mathrm{d}\Omega + \alpha \int_{\Gamma_{su}^I} (u-\bar{u})\delta u \,\mathrm{d}\Gamma = 0. \tag{18}$$

The unknown function u and its variation can be approximated respectively by two different sets of basis functions as follows:

$$u(x,y) = \sum_{J=1}^{\mathrm{NP}} N_J(x,y)u_J, \tag{19}$$

$$\delta u(x,y) = \sum_{I=1}^{NP} \widetilde{N}_I(x,y)v_I, \tag{20}$$

where $N_J(x,y)$ is the above-mentioned RKPM shape function and $\widetilde{N}_I(x,y)$ is the weighting function subordinate to Ith subdomain Ω_s^I:

$$\begin{cases} \widetilde{N}_I(x,y) = 1 & (x,y) \in \Omega_s^I, \\ \widetilde{N}_I(x,y) = 0 & (x,y) \notin \Omega_s^I. \end{cases} \tag{21}$$

Substituting Eqs. (19) and (20) into Eq. (18) and invoking Eq. (21), the third integral in Eq. (18) vanishes directly and Eq. (18) can be shortened and remanipulated as follows:

$$\int_{\Gamma_{su}^I} \left(\alpha u + \frac{\partial u}{\partial x}n_x + \frac{\partial u}{\partial y}n_y\right)\mathrm{d}\Gamma + \int_{\Gamma_{si}^I} \left(\frac{\partial u}{\partial x}n_x + \frac{\partial u}{\partial y}n_y\right)\mathrm{d}\Gamma = \int_{\Gamma_{su}^I} \alpha\bar{u} \,\mathrm{d}\Gamma - \int_{\Gamma_{st}^I} \left(\frac{\partial \bar{u}}{\partial x}n_x + \frac{\partial \bar{u}}{\partial y}n_y\right)\mathrm{d}\Gamma. \tag{22}$$

From Eq. (22) the following discrete equations are obtained straightforwardly:

$$\mathbf{Kd} = \mathbf{R}, \tag{23}$$

where $\mathbf{d} = \{u_1, u_2, \ldots, u_{\mathrm{NP}}\}^{\mathrm{T}}$ is the generalized nodal parameter vector, $\mathbf{K}$ is the $\mathrm{NP} \times \mathrm{NP}$ stiffness matrix and $\mathbf{R}$ is the known righthand. $\mathbf{K}$ and $\mathbf{R}$ can be assembled from the following submatrices or subvectors:

$$\mathbf{K} = [K_{IJ}],$$

and

$$\mathbf{R} = [R_I]$$

in which

$$K_{IJ} = \int_{\Gamma_{su}^I} \left(\alpha N_J + \frac{\partial N_J}{\partial x}n_x + \frac{\partial N_J}{\partial y}n_y\right)\mathrm{d}\Gamma + \int_{\Gamma_{si}^I} \left(\frac{\partial N_J}{\partial x}n_x + \frac{\partial N_J}{\partial y}n_y\right)\mathrm{d}\Gamma, \tag{24}$$

$$R_I = \int_{\Gamma^I_{su}} \alpha\bar{u}\,\mathrm{d}\Gamma - \int_{\Gamma^I_{st}} \left(\frac{\partial \bar{u}}{\partial x}n_x + \frac{\partial \bar{u}}{\partial y}n_y\right)\mathrm{d}\Gamma. \tag{25}$$

3.2. Subdomain collocation method for linear elasticity problems

The two-dimensional linear elasticity problems can be mathematically posed as

$$\sigma_{ij,j} + b_i = 0, \tag{26}$$

$$u_i = \bar{u}_i \quad \text{on } \Gamma_u, \tag{27}$$

$$t_i = \sigma_{ij}n_j = \bar{t}_i \quad \text{on } \Gamma_t, \tag{28}$$

where σ_{ij} is the Cauchy stress tensor, b_i is the ith component of body force, t_i is the ith component of traction and $\bar{u}_i$ and $\bar{t}_i$ are prescribed displacement and prescribed traction on boundaries Γ_u and Γ_t, respectively. Following the same procedure as for Laplace equation, we start with the local weak form

$$\int_{\Omega^I_s} (\sigma_{ij,j} + b_i)\delta u_i\,\mathrm{d}\Omega + \alpha\int_{\Gamma^I_{su}} (u_i - \bar{u}_i)\delta u_i\,\mathrm{d}\Gamma = 0. \tag{29}$$

By applying the divergence theorem and calling Cauchy's stress law to mind, we obtain the counterpart of Eq. (18) which can be written as

$$\int_{\Gamma^I_{si}+\Gamma^I_{su}} t_i\,\delta u_i\,\mathrm{d}\Gamma + \int_{\Gamma^I_{st}} \bar{t}_i\,\delta u_i\,\mathrm{d}\Gamma - \int_{\Omega^I_s} \sigma_{ij}\frac{\partial \delta u_i}{\partial x_j}\,\mathrm{d}\Omega + \int_{\Omega^I_s} b_i\,\delta u_i\,\mathrm{d}\Omega + \alpha\int_{\Gamma^I_{su}} (u_i - \bar{u}_i)\delta u_i\,\mathrm{d}\Gamma = 0. \tag{30}$$

It is obvious that the third integral appearing Eq. (30) disappear if one uses the same approximation of δu_i as given in Eq. (20) and utilizes the standard definition of weighting function given in Eq. (21). If u_i is approximated by Eq. (19) and introducing the following linear relationship for elasticity

$$\{\mathbf{t}\} = \mathbf{n}\{\boldsymbol{\sigma}\} = \mathbf{nDB}\{\mathbf{d}\}. \tag{31}$$

Discrete equations can be derived from Eq. (30) as

$$\left(\int_{\Gamma^I_{su}} (\alpha\mathbf{u} + \mathbf{nDB})\mathrm{d}\Gamma + \int_{\Gamma^I_{si}} \mathbf{nDB}\,\mathrm{d}\Gamma\right)\mathbf{d} = \int_{\Gamma^I_{su}} \alpha\bar{\mathbf{u}}\,\mathrm{d}\Gamma - \int_{\Gamma^I_{st}} \bar{\mathbf{t}}\,\mathrm{d}\Gamma - \int_{\Omega^I_s} \mathbf{b}\,\mathrm{d}\Omega \quad I = 1, 2, \ldots, \mathrm{NP}, \tag{32}$$

where

$$\mathbf{n} = \begin{bmatrix} n_x & 0 & n_y \\ 0 & n_y & n_x \end{bmatrix}, \tag{33}$$

$$\mathbf{B} = [\mathbf{B}_1, \mathbf{B}_2, \ldots, \mathbf{B}_{\mathrm{NP}}]. \tag{34}$$

The entries of matrix $\mathbf{B}$ are given as

$$\mathbf{B}_J = \begin{bmatrix} \dfrac{\partial N_J}{\partial x} & 0 \\ 0 & \dfrac{\partial N_J}{\partial y} \\ \dfrac{\partial N_J}{\partial y} & \dfrac{\partial N_J}{\partial x} \end{bmatrix}. \tag{35}$$

$\{\mathbf{d}\} = \{\mathbf{d}_1, \mathbf{d}_2, \ldots, \mathbf{d}_{\mathrm{NP}}\}$ is the generalized nodal displacement vector and $\mathbf{D}$ is the elasticity matrix consisting of isotropic elastic material properties. Eq. (32) can be assembled further as the compact matrix form as given by Eq. (23) but with the following submatrices and subvectors:

$$\mathbf{K}_{IJ} = \int_{\Gamma^I_{su}} (\alpha\mathbf{N}_J + \mathbf{nDB}_J)\mathrm{d}\Gamma + \int_{\Gamma^I_{si}} \mathbf{nDB}_J\,\mathrm{d}\Gamma, \tag{36}$$

$$\mathbf{R}_I = \int_{\Gamma^I_{su}} \alpha\bar{\mathbf{u}}\,\mathrm{d}\Gamma - \int_{\Gamma^I_{st}} \bar{\mathbf{t}}\,\mathrm{d}\Gamma - \int_{\Omega^I_s} \mathbf{b}\,\mathrm{d}\Omega \tag{37}$$

in which

$$\mathbf{N}_J = \begin{bmatrix} N_J & 0 \\ 0 & N_J \end{bmatrix}. \tag{38}$$

3.3. Numerical integration based on Voronoi domain partition

One key issue left is how to construct subdomains and how to perform numerical integrations which appear in Eqs. (24) and (25) and (36) and (37) to evaluate stiffness matrix as well as righthand vector. For two-dimensional problems concerned in this paper, the whole domain of interest is decomposed by a Voronoi diagram. A Voronoi cell then can naturally be chosen as the subdomain over which the weighting function is defined. The Voronoi cells do not over-lap and the contour of each Voronoi cell serves as the integration path for the aforementioned boundary integration. This is illustrated in Fig. 1 which shows a representative Voronoi cell corresponding to node I and its associated boundary segments and outward normal. If a node is sprinkled in the interior of the domain, any boundary integration like $\int_{\Gamma^I_s} f(\mathbf{x})\mathrm{d}\Gamma$ along the closed boundary Γ^I_s surrounding the node can be performed

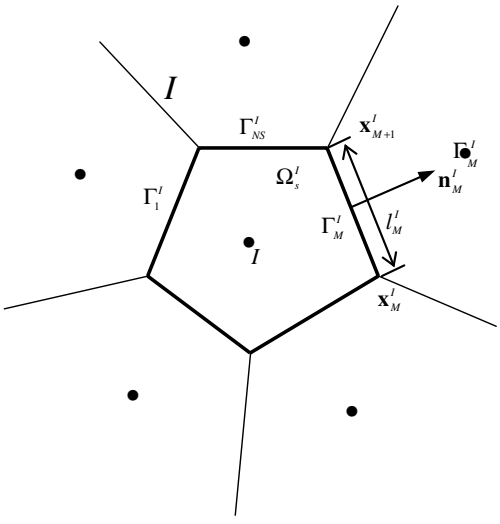

Fig. 1. A representative Voronoi cell for subdomain collocation and integration.

straightforwardly by using the simple two-point trapezoidal rule as [13]:

$$\int_{\Gamma_s^I} f(\mathbf{x})\mathrm{d}\Gamma = \sum_{M=1}^{\mathrm{NS}} \left[\frac{1}{2}\left(l_M^I + l_{M+1}^I\right) f\left(\mathbf{x}_{M+1}^I\right)\right], \tag{39}$$

where as shown in Fig. 1, NS is the total number of segments of Γ_s^I, Γ_M^I are the boundary segments of Γ_s^I, $\mathbf{x}_M^I$ and $\mathbf{x}_{M+1}^I$ are two end points of segment Γ_M^I, l_M^I is the length of the segment Γ_M^I, and $\mathbf{n}_M^I$ is the outward normal of segment Γ_M^I. Note that vertex numbers M are defined recursively as in [13], i.e., $M = \mathrm{NS} + 1 \rightarrow M = 1$.

Once the construction of a Voronoi diagram is completed, the body integration of body force in Eq. (37) can be evaluated directly and accurately by the simplest nodal integration as

$$\int_{\Omega_s^I} \mathbf{b}\,\mathrm{d}\Omega = A_s^I \mathbf{b}(\mathbf{x}^I), \tag{40}$$

where A_s^I is the area of the Voronoi cell with node I as the centroid of the Voronoi cell. In this case, accurately assigning the nodal volume in nodal integration would not remain an issue and Eq. (40) can give rather accurate evaluation of the body integration [15].

4. Numerical examples

4.1. Solution of Laplace equation with Dirichlet and Neumann boundary conditions

The first example considered here is the Laplace equation with Dirichlet and Neumann boundary conditions as given in Eqs. (10)–(15). The problem is solved by a random distribution of 61 nodes to discretize a unit square and the associated Voronoi diagram is shown in Fig. 2. Table 1 shows some of the coordinates and numerical results of part of nodes. Exact solutions given by Eq. (11) are also presented for the purpose of comparison. From Table 1 it is observed that the proposed method can solve Laplace equation with both Dirichlet and Neumann boundary conditions with reasonable accuracy even for randomly distributed nodes.

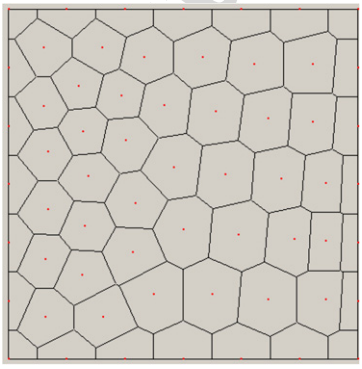

Fig. 2. A 61 nodes Voronoi diagram for a unit square.

Table 1
Exact and numerical results of Laplace equation

Node number	Coordinates		Exact solution	Numerical solution
	x	y		
1	0.0	0.0	0.0	−0.0002
2	1.0	0.0	−1.0	−1.002
3	1.0	1.0	4.0	3.9979
4	0.0	1.0	−1.0	−0.9977
5	0.1667	0.0	−0.0046	−0.0043
6	1.0	0.3333	0.2961	0.2964
7	0.6667	1.0	2.0372	2.0385
8	0.0	0.3333	−0.0370	−0.0371
9	0.6219	0.5299	0.7494	0.7504
10	0.2197	0.3818	0.0851	0.0853
11	0.6599	0.3571	0.3861	0.3870
12	0.3647	0.4468	0.2590	0.2592
13	0.7425	0.1717	−0.0648	−0.0644
14	0.4735	0.5491	0.5259	0.5279

4.2. Patch test for linear elasticity problems

Two patch tests are performed to check the consistency of the present method, and the details of these two patch tests are referred to [1]. The first patch test is the standard patch test. The displacements were prescribed on all outside of a unit square by a linear function of x and y, $u = v = x + y$ in this paper. The unit square was also discretized by the same set of 61 nodes as shown in Fig. 2. The standard patch test requires that the displacements at any point inside the patch satisfy

$$u = v = x + y. \tag{41}$$

The subdomain collocation method presented in this paper satisfies this patch test exactly and some of the results are shown in Table 2. With material properties Young's modulus $E = 1$ and Poisson's ratio $\gamma = 0.25$ assumed, constant stresses were produced at the point inside the domain, i.e., $\sigma_x = \sigma_y = 1.3333$ and $\tau_{xy} = 0.8$.

The second patch test is the so-called high order patch test in [1]. Also the unit square shown in Fig. 2 was used for study. The right side was enforced by a uniform tension of unit intensity, the left side and the bottom side of the square were imposed by symmetry boundary conditions, and the top side of the square was free. The exact solution for this problem with $E = 1$ and $\gamma = 0.25$ is $u = x$ and $v = -y/4$. The proposed subdomain method satisfies this patch test exactly and the results are omitted herein.

4.3. Convergence study of two elasticity problems

Two benchmark elasticity problems are chosen here for the purpose of convergence study of the proposed subdomain collocation method. The first benchmark problem is the cantilever beam problem as shown schematically in Fig. 3. This problem has been studied in many meshless literatures [1,4,7,9,12] and the exact solutions

Table 2
The results of the standard patch test

Node number	Coordinates		u	v
	x	y		
1	0.6219	0.5299	1.1518	1.1518
2	0.2197	0.3818	0.6015	0.6015
3	0.6599	0.3571	1.0170	1.0170
4	0.3647	0.4468	0.8115	0.8115
5	0.7425	0.1717	0.9142	0.9142
6	0.4735	0.5491	1.0226	1.0226

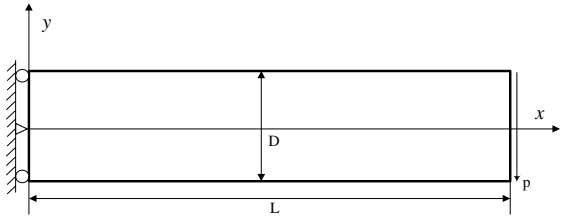

Fig. 3. The cantilever beam problem.

given by Timoshenko and Goodier [18] are summarized as

$$u = \frac{Py}{6\overline{E}I}\left[(6L-3x)x + (2+\bar{\gamma})(y^2 - D^2/4)\right], \tag{42}$$

$$v = \frac{-P}{6\overline{E}I}\left[3\bar{\gamma}y^2(L-x) + (4+5\bar{\gamma})D^2x/4 + (3L-x)x^2\right], \tag{43}$$

$$\sigma_x = \frac{P(L-x)y}{I}, \tag{44}$$

$$\sigma_y = 0, \tag{45}$$

$$\sigma_{xy} = \frac{P}{2I}(y^2 - D^2/4), \tag{46}$$

where P denotes the applied shear force and $I = D^3/12$ denotes the moment of inertia of the beam. For plane stress problems $\overline{E}$ and $\bar{\gamma}$ are replaced by E and γ in Eqs. (42) and (43), while for plane strain problems $\overline{E} = E/(1-\gamma^2)$ and $\bar{\gamma} = \gamma/(1-\gamma)$ are substituted into these equations. The problem was solved for the plane strain case with $P = 1000$, $E = 3.0 \times 10^7$, $\gamma = 0.3$, $D = 2$ and $L = 16$.

Both regular and irregular node distribution strategies were used to discretize the domain to carry out convergence study. Two L_2 errors of energy norm and displacement are calculated in convergence study of the cantilever beam problem and the results are presented in Fig. 4. The L_2 errors of energy norm and displacement are defined as [1]

Error in energy in the L^2 norm

$$= \left\{\frac{1}{2}\int_\Omega \left(\boldsymbol{\varepsilon}^{\mathrm{NUM}} - \boldsymbol{\varepsilon}^{\mathrm{EXACT}}\right)^{\mathrm{T}}\mathbf{D}\left(\boldsymbol{\varepsilon}^{\mathrm{NUM}} - \boldsymbol{\varepsilon}^{\mathrm{EXACT}}\right)\mathrm{d}\Omega\right\}^{1/2}, \tag{47}$$

Error in displacement in the L^2 norm

$$= \left\{\int_\Omega \left(\mathbf{u}^{\mathrm{NUM}} - \mathbf{u}^{\mathrm{EXACT}}\right)^{\mathrm{T}}\left(\mathbf{u}^{\mathrm{NUM}} - \mathbf{u}^{\mathrm{EXACT}}\right)\mathrm{d}\Omega\right\}^{1/2}, \tag{48}$$

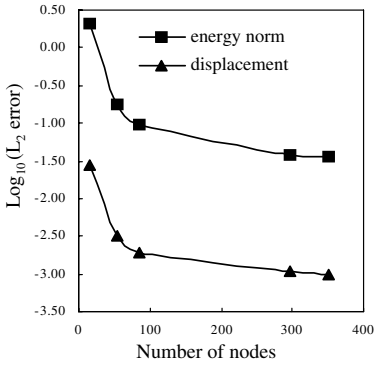

Fig. 4. Convergence rates of the cantilever beam problem.

where the $\boldsymbol{\varepsilon}^{\mathrm{NUM}}$ and $\mathbf{u}^{\mathrm{NUM}}$ are the strain and the displacement obtained by numerical method and the $\boldsymbol{\varepsilon}^{\mathrm{EXACT}}$ and $\mathbf{u}^{\mathrm{EXACT}}$ are the exact solution of the strain and the displacement. Different node distribution strategies were utilized to perform convergence study. Fig. 5 illustrates four different node distributions and the associated Voronoi diagrams which correspond to 15 nodes, 55 nodes, 96 nodes and 215 nodes, respectively. It is noted that for regular node distribution the corresponding Voronoi cells degenerate into regular rectangles while for irregular node distribution the resultant Voronoi diagrams are of the standard forms given in Fig. 1.

Figs. 6 and 7 show the normal stress σ_x and shear stress σ_{xy} at $x = L/2 = 8$ obtained by the present method. The exact solutions are also included for comparison. It is noted from Fig. 7 that the shear stress obtained by present method satisfies the traction-free boundary conditions (i.e. $y = 1$ and $y = -1$) very well. And both the normal stress and shear stress given by present method have an excellent agreement with the analytical solutions.

The second elastostatics problem chosen for convergence study is the problem of a hole in an infinite plate. It is a portion of an infinite plate with a central circular hole subjected to a directional tensile load of 1.0 in the x direction. Only the upper right quadrant of the plate was modeled and shown in Fig. 8 with symmetry conditions were imposed on the left and bottom edges. The prescribed values of σ_x and σ_y along the right edge and the top edge are given by analytical solutions and the details are referred to [1]. The convergence study of this problem is carried out in a similar way and the result is presented in Fig. 9.

4.4. Analysis of a connecting rod with multiple cavities

Analysis of a connecting rod with multiple cavities is chosen deliberately to demonstrate the effectiveness of the present method to treat problems with complicated boundaries. The dimensions and the loading conditions of the connecting rod are illustrated in Fig. 10 with $h_1 = 25$ mm, $h_2 = 15$ mm, $r_1 = 10$ mm, $r_2 = 5$ mm and uniform pressure $p = 30717$ N/mm. The connecting rod is discretized by 215 nodes and the corresponding Voronoi diagram is presented

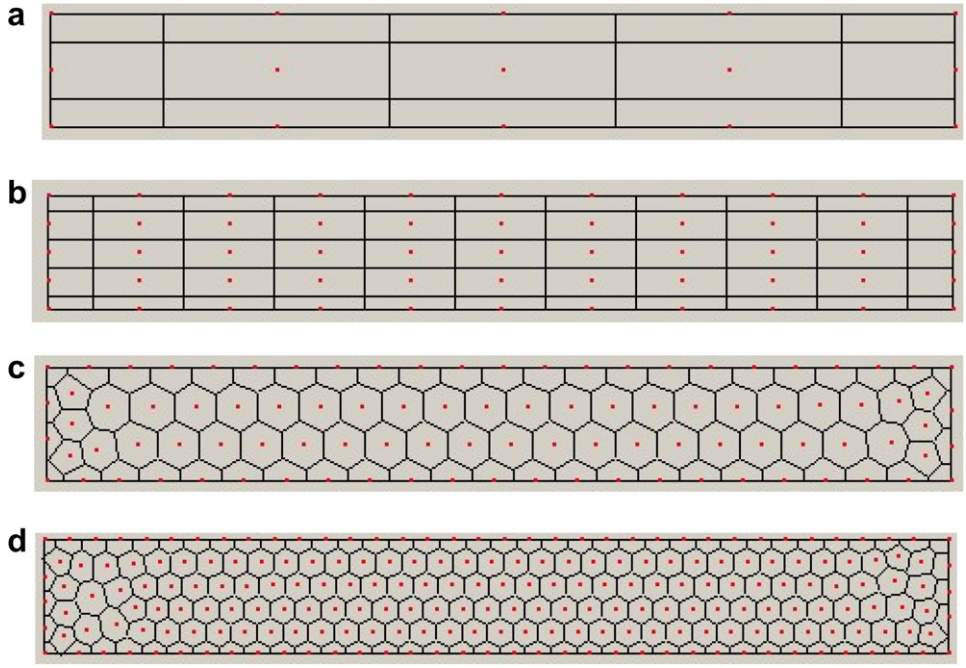

Fig. 5. Four different node distribution strategies and corresponding Voronoi diagrams. (a) Regular distribution of 15 nodes, (b) regular distribution of 55 nodes, (c) irregular distribution of 96 nodes, (d) irregular distribution of 215 nodes.

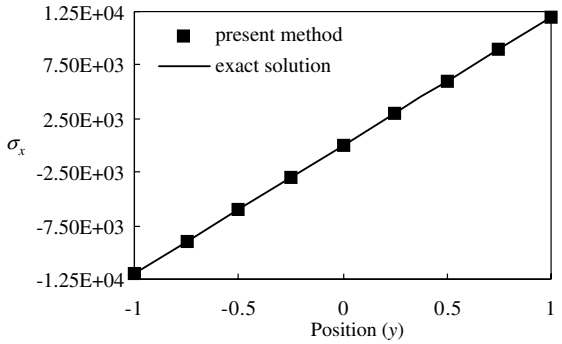

Fig. 6. Comparison of normal stress at the center of the beam ($x = 8$).

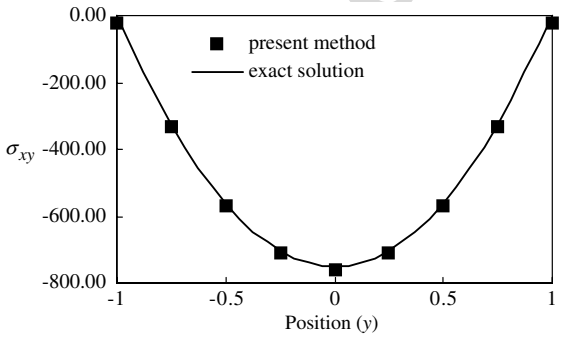

Fig. 7. Comparison of shear stress at the center of the beam ($x = 8$).

in Fig. 11. The problem was solved concerning the steel material property, i.e., $E = 2.1 \times 10^{11}$ and $\gamma = 0.3$. The

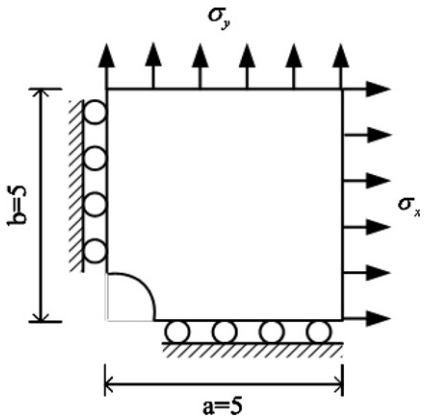

Fig. 8. A portion of an infinite plate with a central hole.

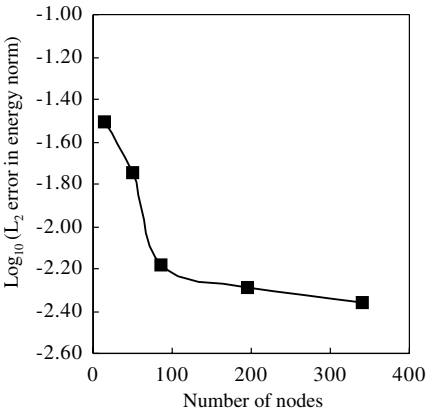

Fig. 9. Convergence rates of the infinite plate with a hole.

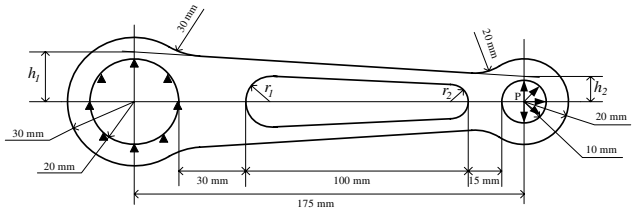

Fig. 10. The dimensions and loading conditions of a connecting rod.

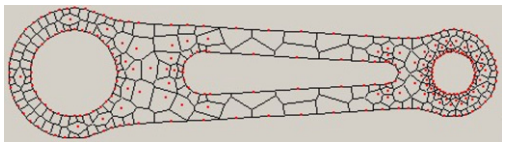

Fig. 11. The Voronoi diagram of a rod discretized by 215 nodes.

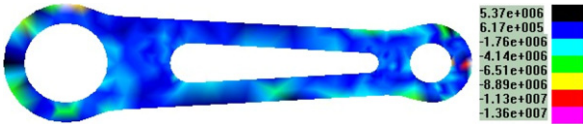

Fig. 12. Distribution of normal stress σ_x.

Fig. 13. Distribution of Von-Mises stress.

obtained normal stress σ_x and the Von-Mises stress are presented in Figs. 12 and 13, respectively.

4.5. h-adaptivity by the subdomain collocation method

A noteworthy feature of the present subdomain collocation method based on Voronoi domain partition is that it provides a natural structure for performing h-adaptivity. Once the high stress gradient regions are predicted in some way, the background Voronoi diagram provides a natural reference structure to insert additional nodes. For example, if one node is recognized as a node within the high gradient region, the vertices of the corresponding Voronoi cell which surrounds this node can be chosen straightforwardly as the additional nodes to be inserted. In this way, the refinement of the high gradient can be realized readily. Lu and Chen [19] carried out h-adaptivity analysis in a similar way in the context of SCNI. A detailed discussion of node refinement strategies of h-adaptivity of meshless method is referred to [20].

The prediction of high stress gradient regions, which is another key issue in adaptivity analysis, can be carried out by making full use of the built-in multiresolution feature of RKPM. In multi-scale RKPM, a set of scale functions or shape functions $N(2^m a_0, \boldsymbol{x}-\boldsymbol{s})$ and wavelet functions $\Psi(2^m a_0, \boldsymbol{x}-\boldsymbol{s})$ are defined as follows:

$$N(2^m a_0, \boldsymbol{x}-\boldsymbol{s}) = C(2^m a_0, \boldsymbol{x}-\boldsymbol{s})\omega_d(2^m a_0, \boldsymbol{x}-\boldsymbol{s}), \tag{49}$$

$$\psi(2^{m+1} a_0, \boldsymbol{x}-\boldsymbol{s}) = N(2^m a_0, \boldsymbol{x}-\boldsymbol{s}) - N(2^{m+1} a_0, \boldsymbol{x}-\boldsymbol{s}), \quad m = 0, 1, 2, \ldots, \tag{50}$$

where a_0 is the initial value of dilation parameter, $\omega_d(2^m a_0, \boldsymbol{x}-\boldsymbol{s})$ and $C(2^m a_0, \boldsymbol{x}-\boldsymbol{s})$ are the kernel function and the correction function corresponding to dilation parameter $2^m a_0$. By defining two operators $P_n u(\boldsymbol{x})$ and $Q_m u(x)$, the multi-scale approximation of any function $u(\boldsymbol{x})$ can be performed as follows:

$$u^a(\boldsymbol{x}) = P_n u(\boldsymbol{x}) + \sum_{m=1}^{n} Q_m u(\boldsymbol{x}) \tag{51}$$

in which

$$P_n u(\boldsymbol{x}) = u_n(\boldsymbol{x}) = \sum_{I=1}^{N} C(2^n a_0, \boldsymbol{x}-\boldsymbol{x}_I)\omega_d(2^n a_0, \boldsymbol{x}-\boldsymbol{x}_I)u(\boldsymbol{x}_I), \tag{52}$$

$$Q_m u(x) = w_m(\boldsymbol{x}) = \sum_{I=1}^{N} \psi(2^m a_0, \boldsymbol{x}-\boldsymbol{x}_I)u(\boldsymbol{x}_I), \quad m = 0, 1, 2, \ldots \tag{53}$$

Note that the low scale solutions $u_n(\boldsymbol{x})$ describe the overall characteristics of the solution while the high scale wavelet solutions $w_m(x)$ predict the local high gradient solution and can be used as the indicator of h-adaptivity. In this way, the displacement, the strain and the stress can also be decomposed into different components corresponding to different scales. For example, the stress can be decomposed as

$$\sigma_{ij} = P_n \sigma_{ij} + \sum_{m=1}^{n} Q_m \sigma_{ij}. \tag{54}$$

The high scale stress solution $Q_m \sigma_{ij}$ can be used to indicate the location of high stress gradient. Although a multi-scale analysis can be performed in this manner, a two-scale decomposition is enough for real adaptivity analysis as in [20,21]. It should be noted that performing adaptivity in this way does not need any posteriori estimation. This constitutes an advantage over the FEM, in which an extra posteriori evaluation process is always needed in adaptivity analysis.

To show the feasibility of h-adaptivity of present method, a L-shaped plate with a uniform tensile load applied on one edge is analyzed. The dimensions, the

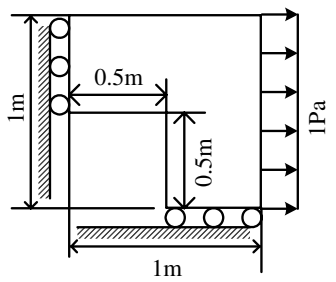

Fig. 14. The computational model of a L-shaped plate.

Fig. 15. Three adaptivity analysis procedure of a L-shaped plate: (a) 96 nodes, (b) 147 nodes, (c) 222 nodes.

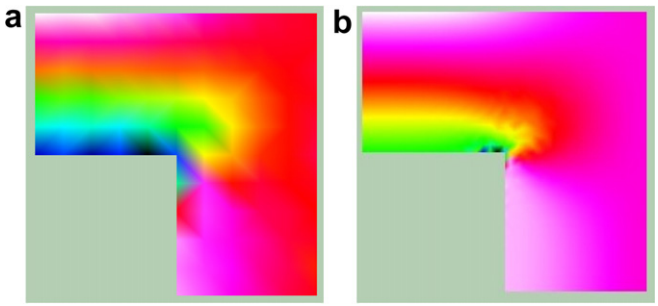

Fig. 16. The initial and the final refined distribution of the normal stress. (a) Initial distribution of normal stress σ_x, (b) final refined distribution of normal stress σ_x.

loading condition, and the boundary conditions are shown in Fig. 14. An initial node distribution of 96 regularly scattered nodes to discretize the domain of interest. A refined 147 nodes distribution is obtained after one step of adaptivity analysis, and finally after four steps of adaptivity analysis a 222 nodes distribution is obtained. These three node distributions are shown in Fig. 15, in which Fig. 15(a)–(c) correspond to the initial, the intermediate and the finial node distribution, respectively. Fig. 16(a) and (b) gives the stress contour of normal stress σ_x corresponding to initial and finial refined node distribution. The material properties used in this analysis is $E = 1.0 \times 10^7$ and $\gamma = 0.3$. It is clearly that the adaptivity of the present method is feasible and effective. The refinement of analysis in this way can locate stress concentration regions more accurately and present a rather clear "edge detection" of high gradient regions.

5. Concluding remarks

A subdomain collocation method based on Voronoi diagram is proposed. The trial function is approximated by the reproducing kernel approximation in a meshless manner, while the test function is interpolated via another set of constant valued weighting functions defined over each of Voronoi cell. In this regard, the present method is in some sense a Petrov–Galerkin method and shape functions and weighting functions are defined over different spaces as in MLPG. The weighting functions, however, are defined over non-overlapping subdomains, which constitutes a principal difference between the two methods. In contrast to point collocation meshless method, the weak form rather than the strong form is solved in subdomain collocation method and the cost of construction of higher order derivatives of shape functions is saved. Furthermore, it is no need to treat traction free boundaries as in a standard Galerkin method, while in all point collocation methods all boundaries including the traction free boundaries must be imposed explicitly. As compared with other Galerkin meshless methods, the need for a quadrature structure is eliminated and the high CPU cost required in Gaussian quadrature of Galerkin meshless methods is avoided. The body integration is converted into contour integration along the boundary of a Voronoi cell. Since all boundary segments of Voronoi cells are located either inside the domain or on the global boundaries, the numerical integration in this method can, wherever the nodes are located inside the domain or on the boundaries, be realized by a much cheaper two-point or three-point trapezoidal rule. Another prominent feature of the present method is that the background Voronoi cells provide a natural structure and h-adaptivity analysis can be performed in a more natural and straightforward way. The Laplace equation and some benchmark linear elasticity problems are chosen as examples to demonstrate the correctness of the proposed method and investigate the convergence property of the method. A multiply connected connecting rod is analyzed to show its performance to deal with complicated problems. Finally, a L-shaped structure is adopted to verify the effectiveness of present method to perform h-adaptivity analysis.

At a cost of construction of background Voronoi cells, to tell the truth, the proposed method is not truly meshless. However, we believe the proposed method provides a new alternative from a standpoint of efficiency, easiness of performing h-adaptivity and other features. Future researches including further development of present method for large deformation and treatment of volume locking are under consideration.

Acknowledgement

The support of this research by Natural Science Foundation of China under grant numbers 10572112 and 10202018 is gratefully acknowledged.

References

[1] T. Belytschko, Y.Y. Lu, L. Gu, Element-free Galerkin methods, Int. J. Numer. Methods Engrg. 37 (1994) 229–256.

[2] W.K. Liu, S. Jun, Y.F. Zhang, Reproducing kernel particle methods, Int. J. Numer. Methods Engrg. 20 (1995) 1081–1106.

[3] J.M. Melenk, I. Babuska, The partition of unity finite element method: basic theory and applications, Comput. Methods Appl. Mech. Engrg. 139 (1999) 289–314.

[4] S.N. Atluri, H.G. Kim, J.Y. Cho, A critical assessment of the truly meshless local Petrov–Galerkin (MLPG) and local boundary integral equation (LBIE) methods, Comput. Mech. 24 (1999) 348–372.

[5] J.J. Monaghan, An introduction to SPH, Comput. Phys. Commun. 48 (1988) 89–96.

[6] C.A. Duarte, J.T. Oden, hp clounds—a meshless method to solve boundary-value problems, Technical Reprot 95-05, Texas Institute for Computational and Applied Mathematics, University of Texas at Austin, 1995.

[7] N.R. Aluru, A point collocation method based on reproducing kernel approximations, Int. J. Numer. Methods Engrg. 47 (2000) 1083–1121.

[8] X. Zhang, K.Z. Song, M.W. Lu, X. Liu, Meshless methods based on collocation with radial basis functions, Comput. Mech. 26 (2000) 333–343.

[9] O.C. Zienkiewicz, R.L. Taylor, The Finite Element Method, fourth ed., McGraw-Hill, London, 1991.

[10] J.R. Shewchuk, Delaunay refinement algorithms for triangular mesh generation, Comput. Geomet. 22 (2002) 21–74.

[11] J. Ruppert, A Delaunay refinement algorithm for quality 2-dimensional mesh generation, J. Algorithms 18 (1995) 548–585.

[12] J. Dolbow, T. Belytschko, Volumetric locking in the element free Galerkin method, Int. J. Numer. Methods Engrg. 46 (1999) 925–942.

[13] J.S. Chen, C.T. Wu, S. Yoon, Y. You, A stabilized conforming nodal integration for Galerkin mesh-free methods, Int. J. Numer. Methods Engrg. 50 (2001) 435–466.

[14] J.S. Chen, S. Yoon, C.T. Wu, Non-linear version of stabilized conforming nodal integration for Galerkin mesh-free methods, Int. J. Numer. Methods Engrg. 53 (2002) 2587–2615.

[15] J.X. Zhou, J.B. Wen, H.Y. Zhang, L. Zhang, A nodal integration and post-processing technique based on Voronoi diagram for Galerkin meshless methods, Comput. Methods Appl. Mech. Engrg. 192 (2003) 3831–3843.

[16] J.X. Zhou, X.M. Wang, Z.Q. Zhang, L. Zhang, On some enrichments of reproducing kernel particle method, Int. J. Comput. Methods 1 (3) (2004) 1–15.

[17] J.X. Zhou, X.M. Wang, Z.Q. Zhang, L. Zhang, Explicit 3-D RKPM shape functions in terms of kernel function moments for accelerated computation, Comput. Methods Appl. Mech. Engrg. 194 (2005) 1027–1035.

[18] S.P. Timoshenko, J.N. Goodier, Theory of Elasticity, third ed., McGraw-Hill, New York, 1970.

[19] H.S. Lu, J.S. Chen, Adaptive Galerkin particle method, Lecture Notes Comput. Sci. Engrg. 26 (2002) 251–267.

[20] Z.Q. Zhang, J.X. Zhou, X.M. Wang, Y.F. Zhang, L. Zhang, h-adaptivity analysis based on multiple scale reproducing kernel particle method, Appl. Math. Mech.-English Edition 26 (2005) 1064–1071.

[21] S.H. Lee, H.J. Kom, Two scale meshfree method for the adaptivity of 3-D stress concentration problems, Comput. Mech. 26 (2000) 376–387.